Konrad-Zuse-Zentrum
für Informationstechnik Berlin

Takustraße 7
D-14195 Berlin-Dahlem
Germany

MICHAEL OEVERMANN[†], RUPERT KLEIN[†]
MARSHA BERGER[‡], JONATHAN GOODMAN[‡]

A Projection Method for Two-Phase Incompressible Flow with Surface Tension and Sharp Interface Resolution

[†] Konrad-Zuse Zentrum
[‡] Courant Institute of Mathematical Sciences, 251 Mercer Street, New York, NY 10027, U.S.A.

ZIB-Report 00–17 (May 2000)

A Projection Method for Two-Phase Incompressible Flow with Surface Tension and Sharp Interface Resolution

Michael Oevermann, Rupert Klein
Konrad-Zuse Zentrum, Takustr. 7, 14195 Berlin, Germany

Marsha Berger, Jonathan Goodman
Courant Institute, 251 Mercer Street, New York, NY 10027, U.S.A.

May 26, 2000

Abstract

We present a fully second order projection method for the simulation of two-phase incompressible flow with surface tension. The Navier-Stokes equations are solved with a projection method on a fixed Cartesian grid. The free interface between the two fluids is tracked with a level set approach. The conditions at the interface for the pressure, the pressure gradient, and the velocity are explicitly incorporated into the scheme leading to a sharp representation of the pressure discontinuity and the interfacial force. The scheme in the presented form does not introduce additional points in the standard finite difference stencils. Computational results are compared with analytic solutions for a static round bubble, damped surface waves, and Rayleigh-Taylor instabilities.

1 Introduction

In this paper we develop a globally second order numerical method for two phase incompressible flows with surface tension and high density and viscosity ratios. Our goal is to have a method that is high order while maintaining sharp interfaces. Previous methods either did not achieve second order accuracy or do so at the cost of spreading the interface or surface tension force over many grid cells. We solve the non-linear Navier-Stokes equations on a uniform Cartesian grid with a projection method. The two fluid phases are coupled by explicit incorporation of the known jump conditions for the pressure into the difference scheme. We perform an asymptotic analysis of the equations in the limit of an infinite density ratio and use the results of this analysis as a guide for the construction of our method. Although our motivation and our asymptotics-based approach to the problem are different from Mayo's [20] or that of LeVeque and Li [18, 19], the resulting numerical scheme has some similarities in the way it incorporates jumps of pressure and pressure gradients. Importantly, we employ the no-slip condition at the interface and the resulting jump condition for both the normal and the tangential pressure gradients to reduce the complexity of the Laplace stencil in the projection step. The current version of the scheme achieves local first, global second order on the basis of a standard-five-point stencil on a Cartesian mesh. The moving interface is tracked via a level set method, and for the solution of the pressure Poisson equations we apply a multi-grid technique.

Two phase incompressible flow plays an important role in many technical applications (like ink-jet printing, fiber production, mixing processes, sprays, fuel combustion, etc.) as well as in many branches of the natural sciences (e.g., dynamics of droplets, instability of stratified flows in the atmosphere, accumulation of pollutants in rain drops). The computation of two-phase incompressible flow with large density ratio and surface tension is a challenging problem and has attracted many researchers over the last years, see [28] and [38] for an overview and detailed reference lists. Numerical methods for two-phase flow can be divided broadly into two classes. In fixed-grid methods the equations are usually solved in the whole domain on a predefined fixed grid. The most popular methods of this type include the volume-of-fluids (VOF) methods [9, 24, 13], level set methods [36, 33], front-tracking schemes [39, 38, 27], and the Marker-and-Cell method [14]. The second class are the moving-grid and Lagrangian methods where a separate, boundary fitted grid is used for each phase [26, 11]. Although moving-grid techniques offer potentially the highest accuracy, they are difficult to apply for complex fully three-dimensional problems or problems with topology changes.

One of the major difficulties in computing two-phase flows is the singular surface tension term in the Navier-stokes equations. In many numerical methods on fixed grids, e.g. [39, 36, 1, 25, 24, 35, 33], the surface tension is taken into account with numerous derivatives of Peskin's immersed boundary method [21]. This method was originally developed to model blood flow in the heart, where the elastic boundary exerts force on the fluid. In the immersed boundary method, singular forces are transferred to the fixed grid using discrete delta functions. By using the discretized discrete delta functions, the discontinuity is spread over several grid cells. Singular forces appear in this method as volume forces. In the context of problems involving surface tension this approach is usually called continuous surface force (CSF) method, which has been introduced by Brackbill et al. in [9]. Tryggvason et al. [38] and Popinet et al. [27] incorporate the surface tension force in a finite volume setting. In their approach the surface tension force is not smeared but is applied solely to the finite volume cell containing the interface. It appears as the product of the surface tension coefficient times the difference between the interface tangents at the boundaries of a control volume.

In the context of solving Poisson's and the biharmonic equation on irregular regions, Mayo in [20] showed a way to explicitly incorporate known jump conditions over discontinuities to get higher order finite difference formulas for the Laplace operator. LeVeque and Li in [18] presented a second order method for elliptic equations with discontinuities and singular sources and, in spirit of Peskin's method, called it the immersed interface method. Their method is very similar to Mayo's approach. These methods offer the framework to construct higher order methods for flows with immersed boundaries and discontinuous solutions by explicitly accounting for discontinuities in the difference scheme. In [19] LeVeque and Li apply their method to solve Stokes flow with elastic boundaries or surface tension. However, to our knowledge an adaption of the method for the full Navier-Stokes equation has not been undertaken yet.

In this paper we present a second order numerical method for the incompressible Navier-Stokes equation for two-phase flow with surface tension. Differently from previous methods solving the Navier-Stokes equation on fixed grids, e.g. [39, 36, 1, 25, 24, 35, 33], we treat the interface as a sharp discontinuity. We achieve this by explicitly incorporating jumps across the interface into the discrete difference operators. The organization of this paper is as follows: In the section 2 we present the governing equations and the asymptotic analysis in the large density ratio limit. In the following section we give the details of our numerical method and in section 4 we show results and convergence studies of numerical experiments.

2 Governing equations

We are looking for a numerical method to solve the incompressible Navier-Stokes equations for two-phase two-dimensional flow with surface tension. In each fluid phase (A) or (B) the momentum and mass-balance equations are

$$\frac{\partial \boldsymbol{u}}{\partial t} + (\boldsymbol{u}\cdot\nabla)\boldsymbol{u} = -\frac{1}{\rho}\nabla p + \nabla\cdot\mathbf{T} - g\,\boldsymbol{e}_g, \tag{1}$$

$$\nabla\cdot\boldsymbol{u} = 0. \tag{2}$$

Here $\boldsymbol{u} = [u, v]^T$ is the velocity, ρ the density, p the pressure, and $\mathbf{T} = \nu\mathbf{D} = \nu(\{\nabla\boldsymbol{u}\} + \{\nabla\boldsymbol{u}\}^T)$ the stress tensor with $[\nabla\cdot\mathbf{D}] = [\Delta\boldsymbol{u}]$. The gravitational force acts with constant g in the direction of the unit vector $\boldsymbol{e}_g$. The boundary conditions at the interface between two immisible viscous fluids are the continuity of the velocity

$$[\![\boldsymbol{u}]\!] = 0, \tag{3}$$

and the dynamic boundary condition balancing the normal and tangential stresses:

$$[\![p]\!] - \boldsymbol{n}\cdot[\![\mu\mathbf{D}]\!]\cdot\boldsymbol{n} = \sigma\kappa, \tag{4}$$

$$\boldsymbol{t}\cdot[\![\mu\mathbf{D}]\!]\cdot\boldsymbol{n} = 0, \tag{5}$$

where σ denotes the surface tension coefficient, κ the curvature, $\boldsymbol{n}$ the normal vector at the interface pointing from fluid (A) into fluid (B), and $\boldsymbol{t}$ the tangential vector. We have introduced here the notation $[\![\cdot]\!] = (\cdot)^{(B)} - (\cdot)^{(A)}$ for any jump across the interface. The continuity of the velocity field together with the momentum equations implies $\left[\!\left[\frac{D\boldsymbol{u}}{Dt}\right]\!\right] = 0$, where $\frac{D}{Dt} = \frac{\partial}{\partial t} + \boldsymbol{u}\cdot\nabla$. Therefore, we get a boundary condition for the pressure gradient in the form

$$\left[\!\left[\frac{1}{\rho}\nabla p\right]\!\right] = [\![\nu\Delta\boldsymbol{u}]\!] \tag{6}$$

which will be an essential ingredient for our numerical method.

For the representation of the moving interface we apply a level set approach. The interface is implicitly given by the zero level of $\phi(\boldsymbol{x}, t)$, where ϕ is defined as the signed normal distance to the interface. The time evolution of the level set follows the advection equation

$$\frac{\partial\phi}{\partial t} + \boldsymbol{u}\cdot\nabla\phi = 0. \tag{7}$$

The value of the level set allows a unique distinction between the two fluid phases. For any quantity ψ we can define

$$\psi(\boldsymbol{x}, t) = \begin{cases} \psi^{(A)}(\boldsymbol{x}, t) & \text{, if} \quad \phi(\boldsymbol{x}, t) < 0 \\ \psi^{(B)}(\boldsymbol{x}, t) & \text{, otherwise} \end{cases} \tag{8}$$

We usually omit the superscript (A) or (B) of the fluid phase, however, from (8) it is always clear to which phase any quantity belongs.

2.1 The governing equations in the limit of a high density ratio

In this study we are particularly interested in two-phase flows with high density ratios. The asymptotic analysis we present here is motivated by problems we initially encountered

solving the theoretically extremely simple problem of a static round bubble with high density ratios, see section 4.1. To investigate the equations in the high density ratio limit

$$\epsilon = \frac{\rho^{(A)}}{\rho^{(B)}} \to 0,$$

we make the equations dimensionless with some reference length l_{ref}, the reference velocity u_{ref}, and the density of the heavy fluid $\rho^{(B)}$. The pressure has been non-dimensionalized with $\rho^{(B)} u_{ref}^2$ and the time with l_{ref}/u_{ref}. For the momentum equations for the light fluid (A) and the heavy fluid (B) we get

$$\frac{D\boldsymbol{u}^{(A)}}{dt} = -\frac{1}{\epsilon}\nabla p^{(A)} + \frac{1}{Re^{(A)}}\Delta \boldsymbol{u}^{(A)} - \frac{1}{Fr^2}\boldsymbol{e}_g, \tag{9}$$

$$\frac{D\boldsymbol{u}^{(B)}}{dt} = -\nabla p^{(B)} + \frac{1}{Re^{(B)}}\Delta \boldsymbol{u}^{(B)} - \frac{1}{Fr^2}\boldsymbol{e}_g, \tag{10}$$

with the Reynolds-numbers $Re^{(A|B)} = u_{ref} l_{ref} \left(\nu^{(A|B)}\right)^{-1}$ and the Froude number $Fr = u_{ref}\left(g l_{ref}\right)^{-1/2}$. We assume that the Reynolds-number of the light fluid remains $O(1)$ as $\epsilon \to 0$. Introducing the asymptotic expansions

$$\begin{array}{rcccccc} \boldsymbol{u}^{(A)} &=& \boldsymbol{u}^{(A,0)} &+& \epsilon\, \boldsymbol{u}^{(A,1)} &+& \dots \\ \boldsymbol{u}^{(B)} &=& \boldsymbol{u}^{(B,0)} &+& \epsilon\, \boldsymbol{u}^{(B,1)} &+& \dots \\ p^{(A)} &=& p^{(A,0)} &+& \epsilon\, p^{(A,1)} &+& \dots \\ p^{(B)} &=& p^{(B,0)} &+& \epsilon\, p^{(B,1)} &+& \dots \end{array} \tag{11}$$

in equation (10) yields the following set of perturbation equations:

$$\begin{array}{lcrcl} \epsilon^{-1} & : & 0 &=& \nabla p^{(A,0)} \\ \epsilon^{0} & : & \dfrac{D\boldsymbol{u}^{(A,0)}}{dt} &=& -\nabla p^{(A,1)} + \dfrac{1}{Re^{(A,0)}}\Delta \boldsymbol{u}^{(A,0)} - \dfrac{1}{Fr^2}\boldsymbol{e}_g \\ & & \dfrac{D\boldsymbol{u}^{(B,0)}}{dt} &=& -\nabla p^{(B,0)} + \dfrac{1}{Re^{(B,0)}}\Delta \boldsymbol{u}^{(B,0)} - \dfrac{1}{Fr^2}\boldsymbol{e}_g \\ \epsilon & : & \dfrac{D\boldsymbol{u}^{(A,1)}}{dt} &=& -\nabla p^{(A,2)} + \dfrac{1}{Re^{(A,1)}}\Delta \boldsymbol{u}^{(A,1)} \\ & & \dfrac{D\boldsymbol{u}^{(B,1)}}{dt} &=& -\nabla p^{(B,1)} + \dfrac{1}{Re^{(B,1)}}\Delta \boldsymbol{u}^{(B,1)}. \end{array} \tag{12}$$

The dynamic boundary condition at the interface presents itself in the asymptotic frame as

$$\begin{array}{lcrcl} \epsilon^{0} & : & \left[\!\left[p^{(0)}\right]\!\right] &=& \boldsymbol{n}\cdot\dfrac{\mathbf{D}^{(B,0)}}{Re^{(B)}}\cdot\boldsymbol{n} + \dfrac{1}{We}\kappa \\ \epsilon^{l} & : & \left[\!\left[p^{(l)}\right]\!\right] &=& \boldsymbol{n}\cdot\left(\dfrac{\mathbf{D}^{(B,l)}}{Re^{(B)}} - \dfrac{\mathbf{D}^{(A,l-1)}}{Re^{(A)}}\right)\cdot\boldsymbol{n} \qquad l \geq 1 \end{array} \tag{13}$$

where $We = \sigma/(\rho_{ref} l_{ref} u_{ref}^2)$ represents the Weber-number. The continuity of the velocity in the viscous case provides us with a boundary condition for the pressure gradient:

$$\begin{array}{lcrcrcl} \epsilon^{-1} & : & \nabla p^{(A,0)} &=& 0 & & \\ \epsilon^{0} & : & \nabla p^{(A,1)} &=& \nabla p^{(B,0)} & - & \left[\!\left[\dfrac{1}{Re}\Delta \boldsymbol{u}^{(0)}\right]\!\right] \\ \epsilon^{1} & : & \nabla p^{(A,2)} &=& \nabla p^{(B,1)} & - & \left[\!\left[\dfrac{1}{Re}\Delta \boldsymbol{u}^{(1)}\right]\!\right] \quad . \end{array} \tag{14}$$

Furthermore, we have at each hierarchical level of the perturbation equations divergence free velocity fields. The main character of the perturbation equations is that it is possible to

solve step by step for each phase separately. The condition of divergence free velocities at each level results in Poisson equations for the respective pressures. Appropriate boundary conditions are to be derived successively from the hierarchy of interface conditions (14) .

To leading order, the pressure $p^{(A,0)}$ in the light phase (A) is constant and the fluid is passively following the movement of the heavy fluid. Knowing the constant pressure $p^{(A,0)}$ we can solve for $\boldsymbol{u}^{(B,0)}$ and $p^{(B,0)}$ with Dirichlet boundary conditions for the pressure Poisson equation given by (13). The next step in the hierarchical system is the solution for $\boldsymbol{u}^{(A,0)}$ and $p^{(A,1)}$ with conditions on the pressure gradient $\nabla p^{(A,1)}$ along the interface provided by equation (14). Note that the solution for the flow of phase A has a gradient boundary condition only. This indicates that a proper implementation of the pressure gradient jump conditions is absolutely necessary to obtain any solution in the low density ratio limit. The strategy continues with $\boldsymbol{u}^{(A,0)}$, $p^{(A,1)} \rightarrow \boldsymbol{u}^{(B,1)}$, $p^{(B,1)} \rightarrow \boldsymbol{u}^{(A,1)}$, $p^{(A,2)} \rightarrow \cdots$. Note that we have always Dirichlet boundary conditions on $p^{(A,l)}$ and Neumann boundary conditions on $p^{(B,l)}$.

The important information to notice here is that all available information at the interface are necessary to solve the asymptotic equations. Most numerical schemes for two-phase flow do not apply any condition on the pressure gradient to solve for the pressure. This means that the kinematic boundary condition on the velocities at the interface is not enforced and spurious unphysical parasitic currents are virtually unavailable. We conclude that the coupling of the pressure gradients on both sides of the interface should be incorporated in a numerical method for two-phase flow with high density ratio. Furthermore, the numerical method should reduce to solving the leading order asymptotic equations if the density of the light fluid is set to zero. In contrast to the development of the immersed interface method [18, 19], our approach to be presented in the following sections is less motivated by the goal to increase the approximation order of the method but rather by the necessity to include all relevant physical information of the underlying problem.

3 Numerical method

For the numerical solution of the momentum equation (1) subject to the incompressibility constraint (2) we use a projection method on cartesian grids. Projection methods for two-phase incompressible and variable density low Mach-number flow have been presented in several papers previously, e.g. [5, 7, 36, 4, 2, 37, 30]. They are all second-order methods and can be traced back to schemes of Harlow and Welch [14] or the projection method of Chorin [15]. These methods methods have in common that they first use an explicit discretization for the effects of convection in a predictor step, and then enforce the compliance with a velocity divergence constraint in a subsequent projection step. They differ in their use of conservative [30]/non-conservative [7, 36, 24, 37] schemes for the momentum equation and in the use of exact [15, 5, 7, 36, 30] or approximate [4, 2] projections.

Our numerical method is similar to these schemes except for the incorporation of the boundary conditions at the interface between the two fluids. Following [6, 3, 30] we apply two projections per timestep: one for the interface velocities and the second one for the cell-centered velocities. For the spatial discretization we use the staggered grid system introduced by Harlow and Welch [14]. Figure 1 shows a grid cell with the index notation and the location of the variables used in the numerical method.

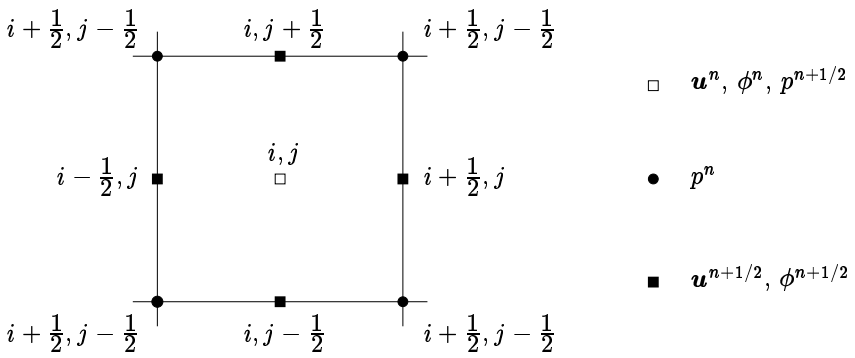

Figure 1: Grid cell with index notation and locations of the variables. □ is the cell center, ▪ are the cell interfaces, and • are the grid nodes.

3.1 Momentum equation

Integrating equation (1) in time between $t = t^n$ and $t = t^{n+1}$ we have for the cell-centered velocities $\boldsymbol{u}_{i,j}$ to second order in time:

$$\begin{aligned} \boldsymbol{u}_{i,j}^{n+1} &= \boldsymbol{u}_{i,j}^{n} - \Delta t \left[[(\boldsymbol{u}\cdot\nabla)\boldsymbol{u}]_{i,j}^{n+\frac{1}{2}} + \frac{1}{\rho_{i,j}^{n+\frac{1}{2}}} [\nabla p]_{i,j}^{n+\frac{1}{2}} - \nu_{i,j}^{n+\frac{1}{2}} [\Delta \boldsymbol{u}]_{i,j}^{n+\frac{1}{2}} + g\boldsymbol{e}_g \right] \\ &= \boldsymbol{u}_{i,j}^{\star} - \frac{\Delta t}{\rho_{i,j}^{n+\frac{1}{2}}} [\nabla p]_{i,j}^{n+\frac{1}{2}} . \end{aligned} \tag{15}$$

The numerical algorithm to advance the velocities from time $t = t^n$ to $t = t^{n+1}$ can be summarized as follows:

1. Computation of the auxiliary interface velocities $\boldsymbol{u}_{i\pm1/2,j\pm1/2}^{\star}$ by Taylor-expansion of the cell centered velocities in space and time.
2. Projection of the auxiliary interface velocities to get divergence free velocities $\boldsymbol{u}_{i\pm1/2,j\pm1/2}^{n+\frac{1}{2}}$ at the cell interfaces.
3. Computation of the auxiliary cell-centered velocities $\boldsymbol{u}_{i,j}^{\star,n+1}$ using $\boldsymbol{u}_{i\pm1/2,j\pm1/2}^{n+\frac{1}{2}}$
4. Projection of the cell-centered velocities to get divergence free cell-centered velocities $\boldsymbol{u}_{i,j}^{n+1}$ at time level $t = t^{n+1}$

Away from the interface our method corresponds to a standard second order projection method. However, at the interface the method differs significantly in how we compute the pressure gradients and therefore how we discretize the discrete Laplace-operator for the pressure Poisson-equation.

3.1.1 Interface velocities

The interface velocities are computed by a Taylor-expansion in space and time of the cell-centered velocities combined with an upwinding process. As an example, we have at the interface $i+\frac{1}{2}, j$, see Figure 1, for the velocity component u normal to the interface:

$$u_{i+\frac{1}{2},j}^{n+\frac{1}{2}} = u_{i+\frac{1}{2},j}^{\star} - \frac{1}{\rho_{i+\frac{1}{2},j}} \left(\frac{\partial p}{\partial x} \right)_{i+\frac{1}{2},j}^{n} . \tag{16}$$

The auxiliary velocity $u^{\star}_{i+\frac{1}{2},j}$ is the time-advanced velocity without the contribution of the pressure gradient. It is determined by a standard upwinding procedure:

$$u^{\star}_{i+\frac{1}{2},j} = \begin{cases} u^{\star,L}_{i+\frac{1}{2},j} & \text{, if } u^{\star,L}_{i+\frac{1}{2},j} > 0 \text{ and } \left(u^{\star,L}_{i+\frac{1}{2},j} + u^{\star,R}_{i+\frac{1}{2},j}\right) > 0 \\ u^{\star,R}_{i+\frac{1}{2},j} & \text{, if } u^{\star,R}_{i+\frac{1}{2},j} < 0 \text{ and } \left(u^{\star,L}_{i+\frac{1}{2},j} + u^{\star,R}_{i+\frac{1}{2},j}\right) < 0 \\ \frac{1}{2}\left(u^{\star,L}_{i+\frac{1}{2},j} + u^{\star,R}_{i+\frac{1}{2},j}\right) & \text{, otherwise.} \end{cases}$$

The values for the auxiliary velocities on the left and right side of the interface are determined by Taylor-expansions in space and time of the cell-centered velocities

$$\begin{aligned} u^{\star,L}_{i+\frac{1}{2},j} &\approx u^{n}_{i,j} + \left(\frac{\partial u}{\partial x}\right)^{n}_{i,j} \frac{\Delta x}{2} + \left(\frac{\partial u}{\partial t}\right)^{\star}_{i,j} \frac{\Delta t}{2}, \\ u^{\star,R}_{i+\frac{1}{2},j} &\approx u^{n}_{i+1,j} - \left(\frac{\partial u}{\partial x}\right)^{n}_{i+1,j} \frac{\Delta x}{2} + \left(\frac{\partial u}{\partial t}\right)^{\star}_{i+1,j} \frac{\Delta t}{2}, \end{aligned} \tag{17}$$

where the time derivatives do not include the pressure gradient. Replacing $\left(\frac{\partial u}{\partial t}\right)^{\star}$ with the momentum equation (1) yields

$$\begin{aligned} u^{\star,L}_{i+\frac{1}{2},j} &\approx u^{n}_{i,j} + \left(\frac{\partial u}{\partial x}\right)^{n}_{i,j} \frac{\Delta x}{2} - \left(u\cdot\nabla u - \nu\Delta u - g e_x\right)^{n}_{i,j} \frac{\Delta t}{2} \\ u^{\star,R}_{i+\frac{1}{2},j} &\approx u^{n}_{i+1,j} - \left(\frac{\partial u}{\partial x}\right)^{n}_{i+1,j} \frac{\Delta x}{2} - \left(u\cdot\nabla u - \nu\Delta u - g e_x\right)^{n}_{i+1,j} \frac{\Delta t}{2}. \end{aligned} \tag{18}$$

For the velocity gradients and the Laplace operator in (18) we apply conventional second order formulas, e.g.

$$\left(\frac{\partial u}{\partial x}\right)_{i,j} \approx \frac{u_{i+1,j} - u_{i-1,j}}{2\Delta x} \quad \text{and} \quad \left(\Delta u\right)_{i,j} \approx \frac{u_{i+1,j} - 2u_{i,j} + u_{i-1,j}}{\Delta x}.$$

For the computations in this study it was not necessary to use limited gradients for the convective terms.

In order to get an equation for the pressure we apply the incompressibility condition on the interface velocities in integral form. For the control volume $\Omega_{i,j}$ with length Δx and Δy around the cell-center i,j we have in discrete form

$$\begin{aligned} \frac{1}{\Delta x \Delta y} \int\limits_{\partial\Omega_{i,j}} \boldsymbol{u}^{n+\frac{1}{2}} \cdot \boldsymbol{n}\, dl &\approx \frac{u^{n+\frac{1}{2}}_{i+\frac{1}{2},j} - u^{n+\frac{1}{2}}_{i-\frac{1}{2},j}}{\Delta x} + \frac{v^{n+\frac{1}{2}}_{i,j+\frac{1}{2}} - v^{n+\frac{1}{2}}_{i,j-1/2}}{\Delta y} \\ &= \left(\nabla\cdot\boldsymbol{u}\right)^{n+\frac{1}{2}}_{i,j} = 0. \end{aligned} \tag{19}$$

At this point it is important to notice that in mixed cells the divergence constraint (19) must incorporate velocities from both fluid phases (A) and (B). Which interface velocity belongs to which fluid phase is uniquely defined by the value of the level set at the corresponding interface location. Using equation (16), it follows from (19) the semi-discrete Poisson equation for the pressure p:

$$\begin{aligned} &\frac{1}{\Delta x}\left(\frac{1}{\rho_{i+\frac{1}{2},j}}\left(\frac{\partial p}{\partial x}\right)_{i+\frac{1}{2},j} - \frac{1}{\rho_{i-\frac{1}{2},j}}\left(\frac{\partial p}{\partial x}\right)_{i-\frac{1}{2},j}\right) \\ + \quad &\frac{1}{\Delta y}\left(\frac{1}{\rho_{i,j+\frac{1}{2}}}\left(\frac{\partial p}{\partial y}\right)_{i,j+\frac{1}{2}} - \frac{1}{\rho_{i,j-\frac{1}{2}}}\left(\frac{\partial p}{\partial y}\right)_{i,j-\frac{1}{2}}\right) = \left(\nabla\cdot\boldsymbol{u}^{\star}\right)_{i,j}. \end{aligned} \tag{20}$$

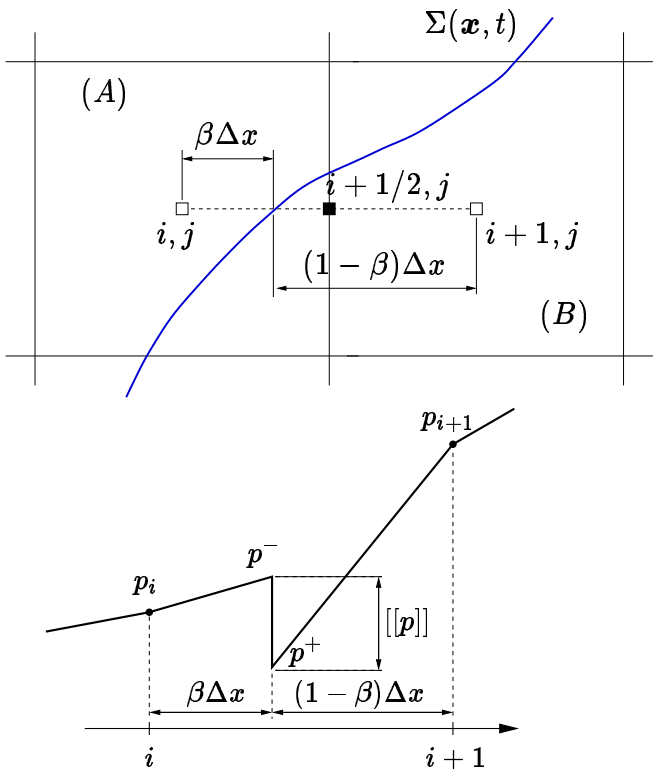

Figure 2: Cut cells and corresponding 1-d pressure distribution along the line connecting the cell-centers i,j and $i+1,j$

The pressure gradients are either evaluated in fluid phase (A) or (B) uniquely defined by the value of the level set at the interface. In the absence of an immersed boundary, standard approximations of the gradients, e.g.

$$\left(\frac{\partial p}{\partial x}\right)_{i+\frac{1}{2},j} = \frac{p_{i+1,j} - p_{i,j}}{\Delta x}$$

lead to the familiar five point stencil for the Laplace-operator.

The pressure gradient with an immersed interface A situation with an interface between the cells i,j and $i+1,j$ is shown in Figure 2, top. According to the asymptotic analysis in the large density ratio limit we want to incorporate the jumps in the pressure and the pressure gradient in our scheme. Knowing these two quantities we are able to construct linear pressure distributions on the left and right side of the interface, see Figure 2, bottom. Assuming that the center of cell (i,j) is in fluid (A) and the cell center of cell $(i+1,j)$ in fluid (B), we can write:

$$
\begin{aligned}
p^- &= p_i + \left(\frac{dp}{dx}\right)^{(A)} \beta\Delta x \\
p^+ &= p_{i+1} - \left(\frac{dp}{dx}\right)^{(B)} (1-\beta)\Delta x \\
[\![p]\!] &= p^+ - p^- \\
\left[\!\left[\frac{1}{\rho}\frac{dp}{dx}\right]\!\right] &= \frac{1}{\rho^{(B)}}\frac{dp^{(B)}}{dx} - \frac{1}{\rho^{(A)}}\frac{dp^{(A)}}{dx}
\end{aligned}
\quad . \tag{21}
$$

These are four equations for the unknowns p^+, p^-, $\frac{dp^{(B)}}{dx}$, and $\frac{dp^{(A)}}{dx}$, which can be solved easily. The jumps $[\![p]\!]$ and $\left[\!\left[\frac{1}{\rho}\frac{dp}{dx}\right]\!\right]$ are given by equation (4) and (6), respectively. The results for the pressure gradients are:

$$
\begin{aligned}
\frac{dp^{(A)}}{dx} &= \frac{\rho^{(A)}}{b\Delta x}\left[p_{i+1,j} - p_{i,j} - [\![p]\!] - (1-\beta)\rho^{(B)}\left[\!\left[\frac{1}{\rho}\frac{dp}{dx}\right]\!\right]\right] \\
\frac{dp^{(B)}}{dx} &= \frac{\rho^{(B)}}{b\Delta x}\left[p_{i+1,j} - p_{i,j} - [\![p]\!] + \beta\rho^{(A)}\left[\!\left[\frac{1}{\rho}\frac{dp}{dx}\right]\!\right]\right]
\end{aligned}
\tag{22}
$$

with $b = \beta\rho^{(A)} + (1-\beta)\rho^{(B)}$. By changing the signs in front of the $[\![p]\!]$ terms we get the formulas for the case with point i,j in fluid (B) and $i+1,j$ in fluid (A). If (A) denotes again the light fluid we get for $\rho^{(A)} = 0$ a zero gradient for the light fluid and the jump in the pressure gradient disappears from the formula for $\frac{dp^{(B)}}{dx}$. In this case the pressure jump $[\![p]\!]$ in $\frac{dp^{(B)}}{dx}$ corresponds to the Dirichlet boundary condition for the heavy fluid in the leading order asymptotic equations. For $\beta = 0$ or $\beta = 1$ the equations (22) reduce to second order central difference stencils for the pressure gradient of fluid phase (B) or fluid (A). Depending on the location of the cell interface $i+\frac{1}{2}, j$ in fluid (A) or fluid (B) we use either $\frac{\partial p^{(A)}}{\partial x}$ or $\frac{\partial p^{(B)}}{\partial x}$ for the approximation of the pressure gradient in equation (20). Since all quantities, except the pressure values $p_{i,j}$ and $p_{i+1,j}$ itself, in (22) are known, using the gradients given in equation (22) do not disturb the standard five point stencil for the discrete Laplace-operator. They do only modify the right hand side of the pressure Poisson equation (20). It is important to keep in mind that the assumption of a viscous fluid gives us jump conditions for the pressure gradient in both x and y directions. This enables the purely one-dimensional approach followed here. In the inviscid case we can derive only a condition for the pressure jump in the normal direction to the interface. Furthermore, since the velocity is continuous across the interface, it seems to be fairly reasonable to use only one velocity at the midpoint of each cell boundary. Note however that jumps in the velocity gradients are not considered here.

The gradients given by (22) are second order only at the midpoints of the corresponding edge in either fluid phase. Since we apply these formulas in the midpoint between the cell-centers, e.g. $(i+\frac{1}{2}, j)$, we expect locally first order of accuracy at the interface. However, convergence studies in section 4 show locally an order of accuracy around 1.5 and globally second order.

Transverse velocities Besides the interface velocities normal to the interfaces we have to approximate the transverse velocities as well. We do this here by simple averaging velocities on the adjacent edges, e.g.

$$
v_{i+\frac{1}{2},j} = \frac{1}{4}\left(v_{i,j+\frac{1}{2}} + v_{i+1,j+\frac{1}{2}} + v_{i,j-\frac{1}{2}} + v_{i+1,j-\frac{1}{2}}\right).
$$

The resulting interpolated velocities still satisfy a discrete divergence free condition:

$$\frac{u_{i+1,j-\frac{1}{2}} - u_{i,j-\frac{1}{2}}}{\Delta x} + \frac{v_{i+\frac{1}{2},j} - v_{i+\frac{1}{2},j-1}}{\Delta y} = 0.$$

3.1.2 Cell-centered velocities

Given the interface velocities we approximate the convective and viscous terms in equation (15) with second order formulas which can be found in textbooks like Peyret and Taylor [22]. For the convective terms we have

$$\left[(\boldsymbol{u}\cdot\nabla)\boldsymbol{u}\right]_{i,j}^{n+\frac{1}{2}} \approx \left[\begin{array}{l} u_{i,j}^{n+\frac{1}{2}} \dfrac{u_{i+\frac{1}{2},j}^{n+\frac{1}{2}} - u_{i-\frac{1}{2},j}^{n+\frac{1}{2}}}{\Delta x} + v_{i,j}^{n+\frac{1}{2}} \dfrac{u_{i,j+\frac{1}{2}}^{n+\frac{1}{2}} - u_{i,j-\frac{1}{2}}^{n+\frac{1}{2}}}{\Delta y} \\ u_{i,j}^{n+\frac{1}{2}} \dfrac{v_{i+\frac{1}{2},j}^{n+\frac{1}{2}} - v_{i-\frac{1}{2},j}^{n+\frac{1}{2}}}{\Delta x} + v_{i,j}^{n+\frac{1}{2}} \dfrac{v_{i,j+\frac{1}{2}}^{n+\frac{1}{2}} - v_{i,j-\frac{1}{2}}^{n+\frac{1}{2}}}{\Delta y} \end{array}\right]$$

with

$$u_{i,j}^{n+\frac{1}{2}} \approx \frac{1}{2}\left(u_{i+\frac{1}{2},j}^{n+\frac{1}{2}} + u_{i-\frac{1}{2},j}^{n+\frac{1}{2}}\right) \quad \text{and} \quad v_{i,j}^{n+\frac{1}{2}} \approx \frac{1}{2}\left(v_{i,j+\frac{1}{2}}^{n+\frac{1}{2}} + v_{i,j-\frac{1}{2}}^{n+\frac{1}{2}}\right).$$

The viscous terms are computed as

$$\left[\Delta\boldsymbol{u}\right]_{i,j}^{n+\frac{1}{2}} \approx \frac{1}{2}\left[\begin{array}{l} \dfrac{u_{i+\frac{1}{2},j}^{n+\frac{1}{2}} - 2u_{i-\frac{1}{2},j}^{n+\frac{1}{2}} + u_{i-\frac{3}{2},j}^{n+\frac{1}{2}}}{\Delta x} + \dfrac{u_{i+\frac{3}{2},j}^{n+\frac{1}{2}} - 2u_{i+\frac{1}{2},j}^{n+\frac{1}{2}} + u_{i-\frac{1}{2},j}^{n+\frac{1}{2}}}{\Delta x} \\ \dfrac{v_{i,j+\frac{1}{2}}^{n+\frac{1}{2}} - 2v_{i,j-\frac{1}{2}}^{n+\frac{1}{2}} + v_{i,j-\frac{3}{2}}^{n+\frac{1}{2}}}{\Delta y} + \dfrac{v_{i,j+\frac{3}{2}}^{n+\frac{1}{2}} - 2v_{i,j+\frac{1}{2}}^{n+\frac{1}{2}} + v_{i,j-\frac{1}{2}}^{n+\frac{1}{2}}}{\Delta y} \end{array}\right].$$

Notice that we neglect here a possible jump of velocity gradients across the interface. Inclusion of this effect will be part of a forthcoming higher order implementation of the present approach. The incompressibility constraint applied to the cell centered velocities at $t = t^{n+1}$ leads to a Poisson equation for the pressure $p^{n+\frac{1}{2}}$ living in the nodes of the computational grid. We define the discrete divergence operator acting on cell-centered velocities as

$$\begin{aligned} (\nabla\cdot\boldsymbol{u})_{i+\frac{1}{2},j-\frac{1}{2}} \quad = \quad & \frac{1}{2} \quad \frac{u_{i,j} + u_{i,j-1} - u_{i-1,j} - u_{i-1,j-1}}{\Delta x} \\ & + \frac{1}{2} \quad \frac{v_{i,j} + v_{i-1,j} - v_{i,j-1} - u_{i-1,j-1}}{\Delta y} \quad . \end{aligned}$$

This divergence operator corresponds to an approximation of a divergence constraint in integral form with a control volume with edges Δx and Δy around node $i+\frac{1}{2}, j-\frac{1}{2}$ Using the same arguments and notation as before, the semi discrete Poisson equation for the pressure at the nodes of the grid is

$$\begin{aligned} & \frac{1}{\Delta x}\left(\frac{1}{\rho_{i+1,j-\frac{1}{2}}} \left(\frac{\partial p}{\partial x}\right)_{i+1,j-\frac{1}{2}} - \frac{1}{\rho_{i,j-\frac{1}{2}}} \left(\frac{\partial p}{\partial x}\right)_{i,j-\frac{1}{2}} \right) \\ + \quad & \frac{1}{\Delta y}\left(\frac{1}{\rho_{i+\frac{1}{2},j}} \left(\frac{\partial p}{\partial y}\right)_{i+\frac{1}{2},j} - \frac{1}{\rho_{i+\frac{1}{2},j-1}} \left(\frac{\partial p}{\partial y}\right)_{i+\frac{1}{2},j-1} \right) = (\nabla\cdot\boldsymbol{u}^{\star})_{i+\frac{1}{2},j-\frac{1}{2}} \end{aligned} .$$

The pressure gradients are computed using the same technique as shown before with the pressure now living in the nodes of the grid. Again, we incorporate explicitly the jumps in

the pressure and the pressure gradient in our scheme. Knowing the pressure in the nodes we can define the pressure gradients for the update of the velocities in equation (15):

$$\left[\nabla p\right]_{i,j} = \begin{bmatrix} \frac{1}{2}\left(\left(\frac{\partial p}{\partial x}\right)_{i,j-\frac{1}{2}} + \left(\frac{\partial p}{\partial x}\right)_{i,j+\frac{1}{2}}\right) \\ \frac{1}{2}\left(\left(\frac{\partial p}{\partial y}\right)_{i-\frac{1}{2},j} + \left(\frac{\partial p}{\partial y}\right)_{i+\frac{1}{2},j}\right) \end{bmatrix}$$

For the numerical solution of the pressure Poisson equations we use an algebraic multigrid preconditioned conjugate gradient method [16]. On the finer grids, n_x, $n_y > 128$, we usually achieve convergence in less than 15 iterations using F-cycles with 4-6 multigrid levels. We did not encounter any convergence problems including surface tension, but the number of iterations usually increases with increasing density ratio.

3.2 Level-set equation

The update of the level-set is achieved with a second order upwind scheme. Integrating equation (7) between $t = t^n$ and $t = t^{n+1}$ we have to second order in time

$$\phi_{i,j}^{n+1} = \phi_{i,j}^{n+1} - \Delta t \left(\boldsymbol{u} \cdot \nabla \phi\right)_{i,j}^{n+\frac{1}{2}} = \phi_{i,j}^{n+1} - \Delta t \left(\nabla \cdot [\boldsymbol{u}\phi]\right)_{i,j}^{n+\frac{1}{2}}.$$

The advection term is discretized as

$$\left(\nabla \cdot [\boldsymbol{u}\phi]\right)_{i,j}^{n+\frac{1}{2}} \approx \frac{u_{i+\frac{1}{2},j}^{n+\frac{1}{2}} \phi_{i+\frac{1}{2},j}^{n+\frac{1}{2}} - u_{i-\frac{1}{2},j}^{n+\frac{1}{2}} \phi_{i-\frac{1}{2},j}^{n+\frac{1}{2}}}{\Delta x} + \frac{v_{i,j+\frac{1}{2}}^{n+\frac{1}{2}} \phi_{i,j+\frac{1}{2}}^{n+\frac{1}{2}} - v_{i,j-\frac{1}{2}}^{n+\frac{1}{2}} \phi_{i,j-\frac{1}{2}}^{n+\frac{1}{2}}}{\Delta y},$$

where u and v are the divergence free interface velocities at time $t^{n+\frac{1}{2}}$. Analogous to the procedure for the interface velocities, the values of the level sets at time $t^{n+\frac{1}{2}}$ at the interface are determined by a Taylor-expansion in space and time to both sides of the interfaces and a subsequent upwinding. As an example, we have for the level set at the interface $i+\frac{1}{2}, j$

$$\phi_{i+\frac{1}{2},j}^{n+\frac{1}{2}} = \begin{cases} \phi_{i+\frac{1}{2},j}^{n+\frac{1}{2},L} & \text{if } u_{i+\frac{1}{2},j}^{n+\frac{1}{2}} > 0 \\ \phi_{i+\frac{1}{2},j}^{n+\frac{1}{2},R} & \text{if } u_{i+\frac{1}{2},j}^{n+\frac{1}{2}} < 0 \\ \frac{1}{2}\left(\phi_{i+\frac{1}{2},j}^{n+\frac{1}{2},R} + \phi_{i+\frac{1}{2},j}^{n+\frac{1}{2},R}\right) & \text{else} \end{cases}$$

where the left sided value of ϕ is given by

$$\begin{aligned} \phi_{i+\frac{1}{2},j}^{n+\frac{1}{2},L} &= \phi_{i,j}^{n} + \left(\frac{\partial \phi}{\partial x}\right)_{i,j}^{n} \frac{\Delta x}{2} + \left(\frac{\partial \phi}{\partial t}\right)_{i,j}^{n} \frac{\Delta t}{2} \\ &= \phi_{i,j}^{n} + \left(\frac{\partial \phi}{\partial x}\right)_{i,j}^{n} \frac{\Delta x}{2} - \left(u_{i,j}^{n} \left(\frac{\partial \phi}{\partial x}\right)_{i,j}^{n} + v_{i,j}^{n} \left(\frac{\partial \phi}{\partial y}\right)_{i,j}^{n}\right) \frac{\Delta t}{2}. \end{aligned}$$

Here, $u_{i,j}^n$ and $v_{i,j}^n$ are the known cell-centered velocity components and the gradients are approximated using unlimited second order gradients, i. e.

$$\left(\frac{\partial \phi}{\partial x}\right)_{i,j} \approx \frac{\phi_{i+1,j} - \phi_{i-1,j}}{2\Delta x} \quad \text{and} \quad \left(\frac{\partial \phi}{\partial y}\right)_{i,j} \approx \frac{\phi_{i,j+1} - \phi_{i,j-1}}{2\Delta y}. \tag{23}$$

The position of the interface is defined as the zero level of ϕ. The β-values in equation (22) are calculated under the assumption of a linear distribution of ϕ between two adjacent grid points. Values of the level set at the nodes of the grid, which are needed for the projection of the cell-centered velocities, are evaluated by taking the arithmetic mean of the four surrounding cell-centered values of ϕ.

To maintain ϕ as the signed normal distance to the front, we reinitialize ϕ after each time step with an area conserving method described in [35, 34] using third order ENO for the spatial and second order Runge-Kutta for the time discretization. All the geometrical information of the front, e.g. the curvature and the normal to the front, are easily obtained to second order from the level sets.

3.3 Boundary conditions

Periodic and inviscid fixed wall boundary conditions are used in this study. We implement boundary conditions via two layers of ghost-cells around the physical domain. In the case of periodic boundaries the rules for filling the ghost-cells are straightforward. For inviscid fixed walls we mirror the velocity at the boundary and extrapolate the level set ϕ via linear extrapolation.

3.4 Time-step restriction

Since our method is an explicit one, we have to restrict the timestep size for stability reasons. We limit the timestep by

$$\Delta t = CFL \cdot \min\left(\Delta t^c, \Delta t^\sigma, \Delta t^g\right)$$

with

$$\Delta t^c = \min_{i,j}\left(\frac{\Delta x}{u_{i,j}}, \frac{\Delta y}{v_{i,j}}\right),\ \Delta t^\sigma = \left(\frac{\overline{\rho} h^3}{\sigma}\right)^{\frac{1}{2}},\ \Delta t^g = \left(\frac{\Delta y}{g}\right)^{\frac{1}{2}}$$

and $\overline{\rho} = \frac{1}{2}(\rho^{(A)} + \rho^{(B)})$ and $h = \min(\Delta x, \Delta y)$. Except the calculations in section 4.3, where we set $CFL = 0.5$, we used a CFL number of 0.75.

3.5 Jump conditions

In order to compute the pressure gradients in equation (22) the jumps given by (4) and (6) must be evaluated. The local values of the normal vector $\boldsymbol{n}$ and the curvature κ are given by

$$\boldsymbol{n} = \frac{\nabla\phi}{|\nabla\phi|} \quad \text{and} \quad \kappa = \nabla\cdot\boldsymbol{n} = \frac{\phi_{xx}\phi_y^2 - 2\phi_{xy}\phi_x\phi_y + \phi_{yy}\phi_x^2}{(\phi_{xx}+\phi_{yy})^{\frac{3}{2}}}.$$

To obtain values at the front $\mathcal{I}$, we linearly interpolate between grid points. For the situation shown in figure 2 we have for example for the curvature:

$$\kappa_{\mathcal{I}} = (1-\beta)\kappa_{i,j} + \beta\kappa_{i+1,j}.$$

The values for $\boldsymbol{n}_{i,j}$ and $\kappa_{i,j}$ at the cell-centers are computed with standard second order difference operators acting on the cell-centered values of ϕ. Similar formulas apply for the second projection, now with values of the level set living in the nodes of the grid, which are always computed by second order interpolation from the cell-centerd values.

The jump in the normal stresses $\boldsymbol{n} \cdot [\![\mathbf{T}]\!] \cdot \boldsymbol{n}$ for the interface shown in figure 2 is

$$\boldsymbol{n}_{\mathcal{I}} \cdot [\![\mathbf{T}]\!] \cdot \boldsymbol{n}_{\mathcal{I}} = \boldsymbol{n}_{\mathcal{I}} \cdot \left(\nu^{(A)} \mathbf{D}_{i,j} - \nu^{(B)} \mathbf{D}_{i+1,j} \right).$$

We compute the deformation tensor with the derivatives given in equation (23). Similar expressions hold for any other interface topology.

4 Results

4.1 Static round bubble

A static round bubble is an interesting test case for any numerical method for two phase flow. Although extremely simple in theory, this test case gives important insight in the production of the so called spurious or parasite currents [28], which can create oscillations strong enough to destroy the interface [17]. It should be noticed that numerical methods using the discrete delta function approach, including the CSF methods, cannot reproduce the exact solution, even if the geometry and the pressure jump are given exactly. The reason is that the pressure discontinuity is approximated by a smooth function where the pressure gradient is non-zero inducing a velocity field. Our method computes the exact solution with zero pressure gradient and zero velocities provided the exact pressure jump is used in equation (21). Figure 3 shows pressure distribution obtained with our method. Clearly seen is the sharp resolution of the discontinuity within one grid cell and the zero pressure gradients in- and outside the bubble. The results of different convergence studies for the spurious currents

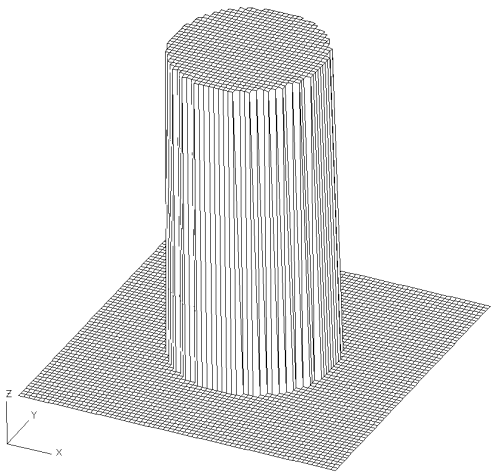

Figure 3: Pressure distribution after one timestep.

are presented in Tables 1, 2, and 3. The diameter of bubble is $d = 1$cm in a computational domain $l_x = l_y = 4$cm. No reinitialization of the level set has been performed. Periodic boundary conditions are used in each direction. The surface tension coefficient corresponds to the surface tension between water and air, $\sigma = 0.072 \frac{\mathrm{N}}{\mathrm{m}}$. The boundary norms $\|u\|_{1,\mathcal{B}}$ are evaluated in the area around the interface defined by $|\phi|_{i,j} \leq \Delta x$. Table 1 shows different norms for the interface velocities after one timestep for a density ratio of $\rho^{(B)}/\rho^{(A)} = 1$. Since we start with an initially zero velocity field, the interface velocities after the first

	$\|u\|_\infty$	q	$\|u\|_1$	q	$\|u\|_2$	q	$\|u\|_{1,\mathcal{B}}$	q
16×16	4.5322e-03	–	4.2577e-04	–	7.7508e-04	–	1.6334e-03	–
32×32	6.3284e-04	2.84	3.8372e-05	3.47	8.6490e-05	3.16	2.5095e-04	2.70
64×64	1.0732e-04	2.55	3.9129e-06	3.29	1.0002e-05	3.11	4.0586e-05	2.63
128×128	2.0307e-05	2.40	3.9088e-07	3.32	1.2085e-06	3.04	7.6760e-06	2.40
256×256	2.8951e-06	2.81	3.5166e-08	3.47	1.3054e-07	3.21	1.2154e-06	2.66

Table 1: Norms of the interface velocity after 1 timestep with convergence rates q for a density ratio $\rho^{(A)}/\rho^{(B)} = 1$. The boundary norms $\|u\|_{1,\mathcal{B}}$ are evaluated in the area around the interface defined by $|\phi| \leq \Delta x$.

timestep are a direct measure for the error in the the pressure gradients. Whereas the convergence rate p in the L^∞ vary between 2.4 - 2.8, we see convergence rates around 3 - 3.5 in the L^1 and L^2 norm. Besides the global 1- and 2-norms, Table 1 shows the velocity error at the interface in the $\|u\|_{1,\mathcal{B}}$ norm. Here, we have defined $\|u\|_{1,\mathcal{B}} = 1/N \sum_{i=1}^{N} \|u\|$, where N is the number of interfaces in the area $|\phi| \leq \Delta x$. The convergence rate varies between 2.4 - 2.7. Similar convergence rates are obtained for a density ratio $\rho^{(B)}/\rho^{(A)} = 1000$, as can be seen in Table 2. Comparable results also hold for the cell-centered velocities after one timestep.

	$\|u\|_\infty$	l	$\|u\|_1$	q	$\|u\|_2$	q	$\|u\|_{1,\mathcal{B}}$	q
16×16	1.7175e-04	–	1.9470e-05	–	3.3593e-05	–	7.7325e-05	–
32×32	2.0412e-05	3.07	1.3908e-06	3.81	3.0056e-06	3.48	9.1590e-06	3.07
64×64	3.9940e-06	2.35	1.4514e-07	3.26	4.0861e-07	2.87	1.9461e-06	2.23
128×128	8.7942e-07	2.18	1.4564e-08	3.31	5.3905e-08	2.92	3.5615e-07	2.45
256×256	1.7811e-07	2.30	1.2908e-09	3.49	6.3717e-09	3.08	6.3264e-08	2.49

Table 2: Norms of the interface velocity after 1 timestep with convergence rates q for a density ratio $\rho^{(A)}/\rho^{(B)} = 1000$. The boundary norms $\|u\|_{1,\mathcal{B}}$ are evaluated in the area around the interface defined by $|\phi| \leq \Delta x$.

Table 3 displays norm of the cell-centered velocities at $t = 0.1$s, corresponding to 4 timesteps on the coarsest grid and 325 on the 256×256 grid. The convergence rates vary between 1.7 and 2.1 in the infinity norm and are nearly identical in the L^∞, L^1, and L^2 norms. In the boundary norm we see convergence rates around 2. The unexpected high convergence rates in the infinity norm and the boundary norm are due to the special character of this test case: since the exact solution is a zero pressure gradient inside and outside the bubble, the location of the interface relative to the grid is not important. The accuracy of the pressure jump alone determines the solution. If we use the exact pressure jump as an input for our numerical method, the result is the exact solution (up to roundoff errors) independent of the β-values determining the interface location. Popinet and Zaleski report in [27] convergence rates around 2.75 with their finite-volume method combined with a front-tracking algorithm for the equal density case including viscosity. However, they do not not provide results for the more interesting case of a high density ratio.

	$\|u\|_\infty$	q	$\|u\|_1$	q	$\|u\|_2$	q	$\|u\|_{1,\mathcal{B}}$	q
16×16	6.3189e-04	–	1.0625e-04	–	1.8651e-04	–	3.4200e-04	–
32×32	1.9184e-04	1.72	2.1883e-05	2.27	4.3071e-05	2.11	8.6257e-05	1.98
64×64	5.4341e-05	1.82	5.5374e-06	1.98	1.0218e-05	2.07	2.3324e-05	1.88
128×128	1.2520e-05	2.11	1.4935e-06	1.89	2.6410e-06	1.95	5.8751e-06	1.98
256×256	3.7718e-06	1.73	2.8768e-07	2.37	5.1084e-07	2.29	1.1689e-06	2.32

Table 3: Norms of the cell-centered velocity at $t = 0.1$s with convergence rates q for a density ratio $\rho^{(A)}/\rho^{(B)} = 1000$. The boundary norms $\|u\|_{1,\mathcal{B}}$ are evaluated in the area around the interface defined by $|\phi| \leq 2\Delta x$.

4.2 Damped surface wave

In this section we present the computations of a surface wave of two superposed viscous fluids and compare the results with the initial value theory of Prosperetti [23]. The initial surface displacement is given by

$$a(x,0) = a_0 \cos(kx)$$

where k is the wavenumber. The initial value solution for two fluids with equal kinematic viscosity ν can be written as [23]

$$\begin{aligned} a(t) &= \frac{4(1-4\beta)\nu^2 k^4}{8(1-4\beta)\nu^2 k^4 + \omega_0^2} a_0 \operatorname{erfc}(\nu k^2 t)^{\frac{1}{2}} \\ &+ \sum_{i=1}^{4} \frac{z_i}{Z_i} \left(\frac{\omega_0^2 a_0}{z_i^2 - \nu k^2} \right) \exp\left((z_i^2 - \nu k^2)t\right) \operatorname{erfc}(z_i t^{\frac{1}{i}}), \end{aligned}$$

where the z_i's are the four roots of the algebraic equation

$$z^4 - 4\beta(k^2\nu)^{\frac{1}{2}} z^3 + 2(1-6\beta)k^2\nu z^2 + 4(1-3\beta)(k^2\nu)^{\frac{3}{2}} z + (1-4\beta)\nu^2 k^4 + \omega_0^2 = 0.$$

The Z_i's are given by $Z_1 = (z_2 - z_1)((z_3 - z_1)(z_4 - z_1)$ with cyclic permutations of the indices for Z_2, Z_3, Z_4. The inviscid oscillation frequency is $\omega_0 = \sigma k/(\rho^{(A)} + \rho^{(B)})$, and the dimensionless parameter β is defined as $\beta = \rho^{(A)}\rho^{(B)}/\left(\rho^{(A)} + \rho^{(B)}\right)^2$.

The computations were carried out for the wavenumber $k = 1$ with an initial amplitude $a_0 = 0.02\, l_x$ on a square grid with $l_x = l_y = 2\pi$. This amplitude corresponds to 5 grid cells on our finest (256×256)-mesh. We use periodic boundary conditions in the horizontal and inviscid fixed wall conditions in the vertical direction.

Table 4 shows the results of a convergence study for the equal density case. We present convergence rates for the cell-centered pressure $p_{i,j}^{n+\frac{1}{2}}$, the cell-centered velocity $u_{i,j}^n$, and the cell-centered level set values $\phi_{i,j}^n$. The convergence rate q for any variable ψ is defined as

$$q = \log_2(r)$$

with

$$r = \frac{|\psi_{4h} - \psi_{2h}|}{|\psi_{2h} - \psi_h|}.$$

Here, $h = \Delta x = \Delta y$ is the grid spacing and ψ_{nh} denotes the solution on the grid with grid spacing nh. In the 1- and 2-norm we have convergence rates around 2 in each variable on the

grids	variable	$q_{\|u\|_\infty}$	$q_{\|u\|_1}$	$q_{\|u\|_2}$
32×32 / 64×64 / 128×128	u	1.74	1.60	1.74
	p	1.66	2.11	2.12
	ϕ	1.63	1.79	1.64
64×64 / 128×128 / 256×256	u	2.26	2.55	2.37
	p	1.48	2.04	2.07
	ϕ	1.89	2.12	1.98

Table 4: Convergence rates for the pressure, the velocity, and the level set function for two grid sequences in different norms at $t = 288$s. $\rho^{(A)} = \rho^{(B)} = 1000\text{kg/m}^3$, $\nu^{(A)} = \nu^{(B)} = 10^{-3}\text{m}^2/\text{s}$, $\sigma = 0.072\text{N/m}$.

finer grid sequence. As expected, the convergence rate for the pressure in the infinity-norm is below two, but with values of $q = 1.66$ and $q = 1.48$ better than the expected first order accuracy in this norm. For the velocity we have second order of accuracy in each norm.

Although we cannot expect a priory convergence towards the analytic solution, it is interesting to compare with it. Table 5 shows a convergence study of the interface location towards the analytic solution. The error $|e|^{\text{linear}}$ is defined as the root mean square of the amplitude difference between the linear theory solution $r^{linear}(t) = r_0 + \epsilon \cos(\omega t)$ and the computed interface location at $\theta = 0$:

$$|e|^{linear} = \left(\int_0^{2T} \left(r^{linear}(t) - r\left(\theta = 0, t\right) \right)^2 dt \right)^{\frac{1}{2}}.$$

At higher grid resolutions we have sublinear convergence to the linear initial value theory. Similar results hold for a density ratio 1/100, which are displayed in Table 6. The sublinear convergence towards the initial value theory indicate that we are not converging towards this solution. The computations of Gueyffier et al. [13] and Popinet and Zaleski [27] showed also only sublinear convergence for this test case. They argued in [27] that the bounded domain in the calculation could be a cause for this discrepancy as the initial value solution is given in the infinite depth case. However, tests with doubling the computational domain in the vertical direction showed an influence on the solutions but they did not change much the convergence towards the analytic solution.

	$\|e\|^{linear}$	q
32×32	8.3102e-4	–
64×64	3.2168e-4	1.37
128×128	1.8624e-4	0.79
256×256	1.0763e-4	0.79

Table 5: Convergence of the error between the computed amplitude $a(t)$ and the amplitude of the linear initial value theory a^{linear}. $\rho^{(A)} = \rho^{(B)} = 1000\text{kg/m}^3$, $\nu^{(A)} = \nu^{(B)} = 10^{-3}\text{m}^2/\text{s}$, $\sigma = 0.072\text{N/m}$.

In Table 7 we show the results of a grid convergence study for a density ratio of 100. The convergence rates do not differ significantly from the convergence rates with equal fluid densities in Table 4. On the finer grid sequence we have second order convergence for the

	$\|e\|^{linear}$	q
32×32	5.4537e-03	–
64×64	3.0289e-03	0.85
128×128	1.7330e-03	0.80
256×256	1.0061e-03	0.79

Table 6: Convergence of the error between the computed amplitude $a(t)$ and the amplitude of the linear theory a^{linear}. Density ratio 1/100, equal kinematic viscosities.

velocity u and the level set ϕ in each norm. The convergence rates for the pressure in the 1- and 2-norm are slightly less than in the equal density case.

grids	variable	$q_{\|u\|_\infty}$	$q_{\|u\|_1}$	$q_{\|u\|_2}$
32×32 / 64×64 / 128×128	u	1.94	2.00	2.07
	p	1.48	1.29	1.89
	ϕ	1.56	2.14	2.25
64×64 / 128×128 / 256×256	u	2.13	2.27	2.37
	p	1.58	1.70	1.83
	ϕ	2.05	2.22	2.01

Table 7: Convergence rates for the pressure, the velocity, and the level set function for two grid sequences in different norms at $t = 570$s. $\rho^{(A)}10\text{kg/m}^3$, $\rho^{(B)} = 1000\text{kg/m}^3$, $\nu^{(A)} = \nu^{(B)} = 10^{-3}\text{m}^2/\text{s}$, $\sigma = 0.072\text{N/m}$.

Figure 4 shows the time evolution of the surface amplitude for the equal density ratio computation and the 1/100 density ratio case. The numerical solution is nearly indistinguishable from the initial value solution for equal density fluids. In the high density ratio case we observe a significant difference in the phase speed between the analytical solution and the calculation. Unfortunately, neither in [27] nor in [13] pictures are shown in the unequal density case. The shift in wave speed increases with increasing density ratio.

4.3 Rayleigh-Taylor instability

A common test problem for numerical methods for two-phase flow is the Rayleigh-Taylor instability, where a heavy fluid is placed on top of a light fluid with a small initial perturbation of the interface between the two fluids. In the literature on numerical methods for two-phase flow on fixed grids one can find many qualitative results for the long time, non-linear evolution of the instability, see for example [12, 38, 9, 27, 24, 7, 25] Surprisingly, from the cited references only Brackbill et al. ccompared in [9] their results for short times quantitatively with the linear theory.

Rayleigh-Taylor instability, short time

For short times an initially sinusoidal disturbance growth according to linear theory exponentially in time as $\exp(nt)$ with a growth rate given by [10]

$$n^2 = kg\left[A - \frac{k^2\sigma}{g\left(\rho^{(A)} + \rho^{(B)}\right)}\right], \tag{24}$$

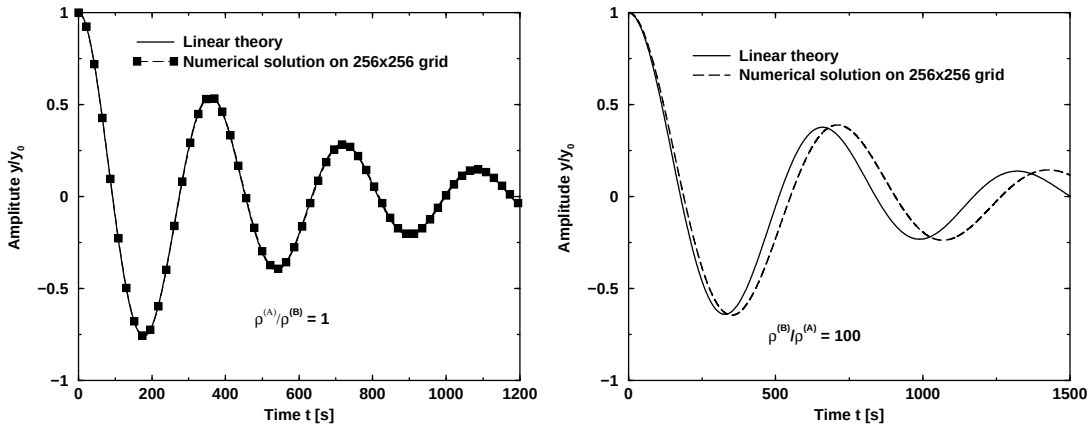

Figure 4: Evolution of the dimensionless amplitude $a(t)/a_0$ for the initial value solution of the linearized equations and the numerical solution. Left: equal density case with $\rho^{(A)} = \rho^{(B)} = 1000\text{kg/m}^3$; right: $\rho^{(A)} = 10\text{kg/m}^3$ and $\rho^{(B)} = 1000\text{kg/m}^3$. The numerical solutions shown are computed on a 256×256 grid with $\nu^{(A)} = \nu^{(B)} = 10^{-3}\text{m}^2/\text{s}$, $\sigma = 0.072\text{N/m}$.

where k is the wave number and A the Atwood number $A = \left(\rho^{(A)} - \rho^{(B)}\right) / \left(\rho^{(A)} + \rho^{(B)}\right)$. With (24) we can define a critical surface tension σ_c for which $n = 0$. Defining the stability parameter

$$\Phi = \frac{\sigma}{\sigma_c},$$

we have stable oscillations of the interface for $\Phi > 1$ and instability with exponential growth for $\Phi < 1$. Figure 5 shows on the left side the time evolution for different values of the stability parameter Φ. Logarithmic amplitude values are shown for the unstable situations and linearly scaled amplitudes for the stable case with $\Phi = 1.0625$. The presented calculations were carried out with an initial sinusoidal surface disturbance of the form $0.02 l_x \cos(kx)$. The computational domain is $l_x = 2\pi$ and $l_y = 2l_x$ with 64×128 grid points. Periodic boundary conditions in the horizontal and fixed wall slip conditions are used in the vertical direction. The density of the heavy and the light fluid are $\rho^{(A)} = 3\frac{\text{kg}}{\text{m}^3}$ and $\rho^{(B)} = 1\frac{\text{kg}}{\text{m}^3}$, respectively, corresponding to an Atwood number of $A = 0.5$. The critical surface tension is $\sigma_c = 20\frac{\text{kg}}{\text{s}^2}$. Figure 5 shows on the right side the dispersion diagram with computed growth rates versus the growth rates given by (24). The numerical growth rates are always a little less than the linear theory but the agreement is quite reasonable. It is quite difficult to perform computations around the critical surface tension. Numerical experiments with a few time-steps showed instability for $\sigma = 19.8\frac{\text{kg}}{\text{s}^2}$ and stability for $\sigma = 20.2\frac{\text{kg}}{\text{s}^2}$, corresponding to values of the stability parameter of $\Phi = 0.99$ and $\Phi = 1.01$. The dispersion diagram provided in [9] shows unphysical instability of their numerical method even for $\Phi = 1.17$.

The results of a convergence study of the exponential growth rate with a constant stability parameter $\Phi = 0.25$ are given in Table 8. The theoretical growth rate is $n^{linear} = 1.9365$. The numerical growth rates are determined by a linear curve fit in the amplitude range of $1.5 \leq \ln(a(t)/a_0) \leq 3.0$. The numerical growth rate on the finest grid is 0.5% below the linear theory.

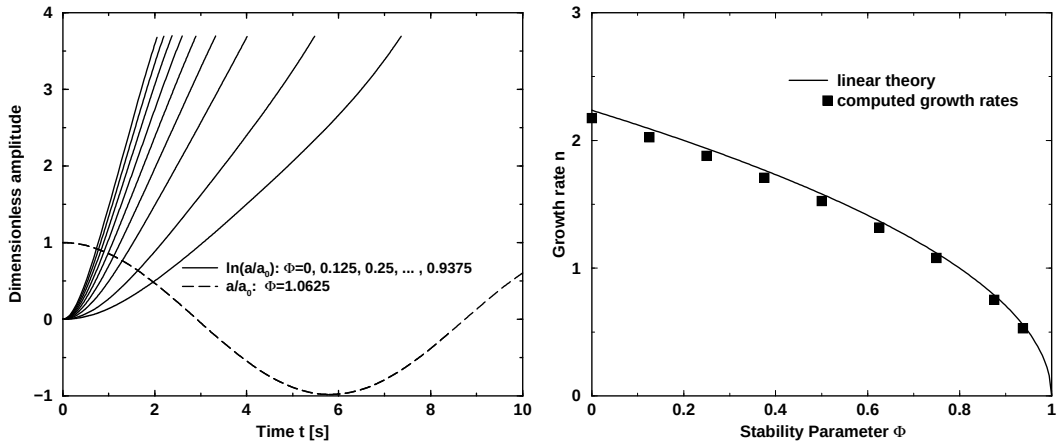

Figure 5: Left: Dimensionless amplitude $a(t)/a_0$ for different values of surface tension parameter $\sigma = 0, 2.5, \ldots, 17.5, 18.75, 21.25$ corresponding to values of the stability parameter $\Phi = 0,\ 0.125,\ 0.25,\ 0.375,\ 0.5,\ 0.625,\ 0.75,\ 0.875,\ 0.9375,\ 1.0625$. Right: Dispersion diagram with computed and theoretical growth rates from linear theory. All computations with $\rho^{(A)}/\rho^{(B)} = 3$ on a 64×128 grid with $l_x = 0.5\ l_y = 2\pi$.

	$\|n - n^{linear}\|$	p
32×64	1.6471e-01	-
64×128	7.9941e-02	1.04
128×256	3.2489e-02	1.30
256×512	9.7474e-03	1.74

Table 8: Convergence of the exponential growth rate n for $\rho_2/\rho_1 = 3$, $\sigma = 0.25\sigma_c$

Rayleigh-Taylor instability, long time

Our last numerical example is the computation of Rayleigh-Taylor instabilities in the long time, non-linear regime. We consider here the example treated in [24, 27]. The densities of the light and the heavy fluid are 0.1694kg/m^3 and 1.225kg/m^3, respectively, while the dynamic viscosity in each fluid is $\mu = 3.13 \cdot 10^{-3}\text{kg/ms}$. The kinematic viscosities are then $\nu^{(A)} = 1.8477 \cdot 10^{-2}\text{m}^2/\text{s}$ and $\nu^{(B)} = 2.5551 \cdot 10^{-3}\text{m}^2/\text{s}$. The computational domain is $l_x = 1\,\text{m}$ and $l_y = 4\,\text{m}$ with a 128×256 grid. We use periodic boundary conditions in the horizontal and fixed wall boundaries in the vertical direction. The initial perturbation is given by $\eta(x) = 0.01 l_x \cos kx$ with $k = 2\pi/l_x$.

Figure 6 shows the interface and velocity vectors at different times. As the heavy fluid penetrates the light fluid is forms a mushroom shaped end pushing the light fluid up. The simulation shows some pinch off of heavy fluid at this grid resolution. The results are in good agreement with pictures presented in [27].

In Figure 7 we repeat the computation above including surface tension with a surface tension coefficient of $\sigma = 0.1337\text{kg/s}^2$. The simulation demonstrates clearly the stabilizing effect of the surface tension – the heavy fluid needs more time to penetrate the light fluid and the heavy fluid pieces after pinch-off show the tendency to form round droplets.

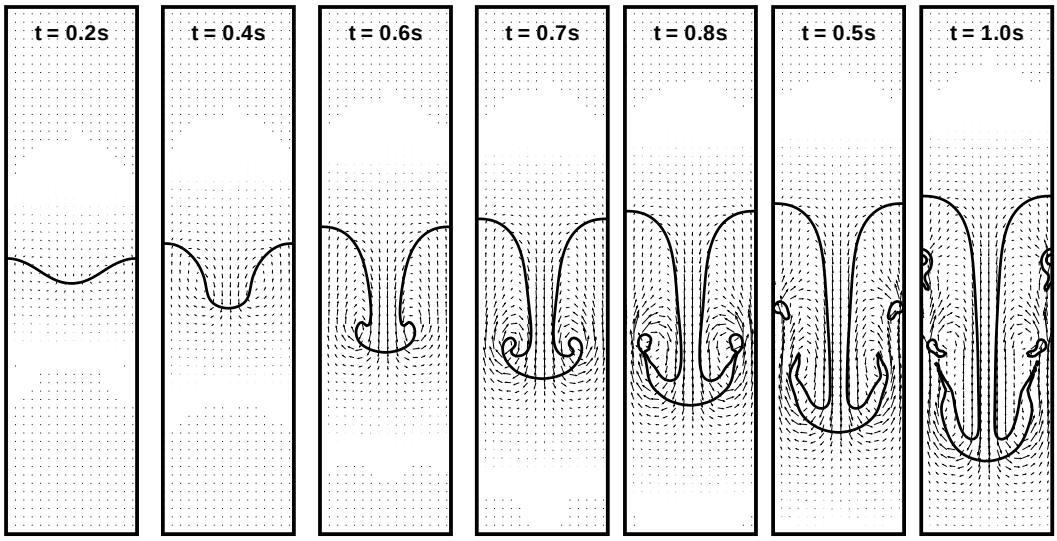

Figure 6: Rayleigh-Taylor instability of an initially sinusoidal perturbation at times $t = 0.2, 0.4, 0.6, 0.7, 0.8, 0.9, 1.0$s. Computational domain is $1\text{m} \times 4\text{m}$ with 64×256 grid points. $\rho^{(A)} = 0.1694\text{kg/m}^3$, $\rho^{(B)} = 1.225\text{kg/m}^3$, $\mu^{(A)} = \mu^{(B)} = 3.13 \cdot 10^{-3}\text{kg/ms}$

5 Conclusion and future work

We have described a new numerical method to solve the incompressible Navier-Stokes equations for two-phase flow with surface tension. Our approach is guided by an asymptotic analysis of the equations in the limit of an infinity density ratio. We explicitly incorporate the jump in the pressure and the pressure gradient into the discretization scheme. Our approach is easy to implement in any projection type method for two-phase flow. In the presented form it modifies only the right hand side in the pressure Poisson equation and does not affect the standard finite difference operators. The computational examples given show that the method has a global approximation order of 2 and that it converges for several test cases towards analytic solutions of linearized problems.

It is tempting to make the method locally as well as globally second order. This can be achieved by taking into account higher than linear pressure distributions in mixed cells or by introducing higher jump conditions for the pressure. This will be the next step in further developments of this method. An open question left by the simulations of the damped surface wave in Section 4.2 is the error in phase speed for high density ratios. It would be interesting to investigate this further to find out the cause for this discrepancy between the initial value solution of the linearized Navier-Stokes equations and the numerical method.

So far we have assumed continuity of the velocity gradients. This is obviously a rough approximation for fluids with different viscosities. The jump condition 5 on the tangential stresses provides some additional information about the jump in the velocity gradient across the interface which could be used to improve the method.

Finally, there is a severe limitation to compute real physical problems with our two-dimensional method. In the future it will be necessary to extend the method to axisymmetric problems and three space dimensions. Other future directions of this work include extending the algorithm for the computation of flows with variable density and surface tension, heat transfer and vaporization, and, eventually, chemical reactions via flame front tracking along

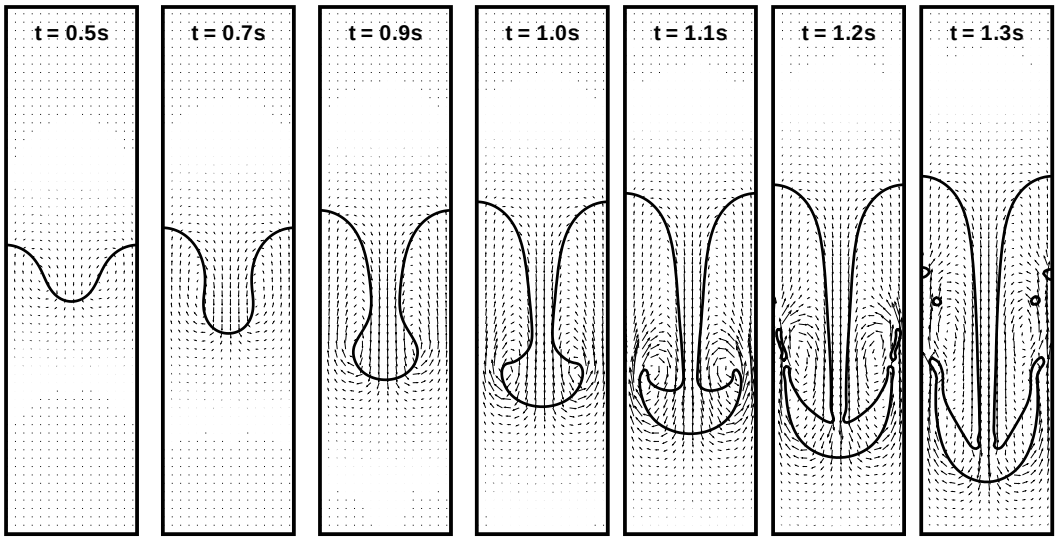

Figure 7: Rayleigh-Taylor instability with surface tension. Everything is initialized the same way as in Fig. 6.

the lines of [32, 37, 29]. Another line of development will be the incorporation of mass conservation corrections in the present level set scheme following ideas of Bourlioux [8], which were implemented so far by and Schneider and Klein [31].

Acknowledgment

The authors gratefully acknowledge the support of the Department of Energy Grant No. DEFG02-88ER25053 and DEFG02-92ER25139, NSF Grant No. DMS 9705380, and NASA Grant No. NAG 5-7583. Furthermore, we thank Thomas Schneider for providing the multigrid code.

References

[1] I. Aleinov and E. G. Puckett. Computing Surface Tension with High-Order Kernels. In M. Hafez and K. Oshima, editors, *Proceedings of the 6th International Symposium on Computational Fluid Dynamics*, volume I, pages 6–13, Lake Tahoe,CA, September 1995.

[2] A. S. Almgren, J. B. Bell, P. Colella, L. H. Howell, and M. L. Welcome. A Conservative Adaptive Projection Method for the Variable Density Incompressible Navier-Stokes Equations. *Journal of Computational Physics*, 142:1–46, 1998.

[3] A. S. Almgren, J. B. Bell, P. Colella, and T. Marthaler. A Cartesian Grid Projection Method For The Incompressible Euler Equations in Complex Geometries. *SIAM J. Sci. Comput.*, 18(5):1289–1309, 1997.

[4] A. S. Almgren, J. B. Bell, and W. G. Szymczak. A Numerical Method for the Incompressible Navier-Stokes Equations Based on an Approximate Projection. *SIAM J. Sci. Comput.*, 17(2):269–282, 1996.

[5] J. B. Bell, P. Colella, and H. M. Glaz. A Second-Order Projection Method for the Incompressible Navier-Stokes Equations. *Journal of Computational Physics*, 85:257–283, 1989.

[6] J. B. Bell, P. Colella, and L. H. Howell. An efficient second-order projection method for viscous incompressible flow. In *Proceedings of the 10th AIAA Computational Fluid Dynamics Conference*, pages 360–367, Honolulu, HI, June 24-27 1991.

[7] J. B. Bell and D. L. Marcus. A Second-Order Projection Method for Variable Density Flows. *Journal of Computational Physics*, 101:334–348, 1992.

[8] A. Bourlioux. A Coupled Level-Set Volume-Of-Fluid Algorithm for Tracking Material Interfaces. *3rd Annual Conference of the CFD Society of Canada*, Banff, Alberta, Canada, June 25-27, 1995.

[9] J. U. Brackbill, D. B. Kothe, and C. Zemach. A Continuum Method for Modeling Surface Tension. *Journal of Computational Physics*, 100:335–354, 1992.

[10] P. G. Drazin and N. H. Reid. *Hydrodynamic Stability.* Cambridge University Press, Cambridge, 1981.

[11] D. E. Fyfe, E. S. Oran, and M. J. Fritts. Surface tension and Viscosity with Lagrangian Hydrodynamics on a Triangular Mesh. *Journal of Computational Physics*, 76:349–384, 1987.

[12] J. Glimm, O. McBryan, R. Menikoff, and D.H̃. Sharp. Front tracking applied to rayleigh-taylor instability. *SIAM J. Sci. Stat. Comput.*, 7(1):230–251, 1986.

[13] D. Gueyffier, J. Li, A. Nadim, R. Scardovelli, and S. Zaleski. Volume-of-Fluid Interface Tracking with Smoothed Surface Stress Methods for Three-dimensional Flows. *Journal of Computational Physics*, 152:423–456, 1999.

[14] F. H. Harlow and J. E. Welch. Numerical calculation of time-depemdent viscous incompressible flow of fluid with a free interface. *The Physics of Fluids*, 8:2182–2189, 1965.

[15] Chorin A. J. A numerical method for solving incompressible viscous flow problems. *Journal of Computational Physics*, 2:12–26, 1967.

[16] F. Kickinger. Algebraic multigrid for discrete elliptic second order problems. Technical Report 513, Institut für Mathematik, Universität Linz, 1997.

[17] B. Lafaurie, C. Nardone, R. Scardovelli, S. Zaleski, and G. Zanetti. Modelling Merging Fragmentation in Multiphase Flows with SURFER. *Journal of Computational Physics*, 113:134–147, 1994.

[18] R. J. LeVeque and Z. Li. The Immersed Interface Method for Elliptic Equations with Discontinuous Coefficients and Singular Sources. *SIAM Journal on Numerical Analysis*, 31(4):1019–1044, 1994.

[19] R. J. LeVeque and Z. Li. Immersed Interface Methods for Stokes Flow with Elastic Boundaries or Surface Tension. *SIAM Journal on Scientific Computing*, 18:709–735, 1997.

[20] A. Mayo. The Fast Solution of Poisson's and the Biharmonic Equation onIrregular Regions. *SIAM Journal on Numerical Analysis*, 21(2):285–299, 1984.

[21] C. S. Peskin. Numerical analysis of blood flow in the heart. *Journal of Computational Physics*, 25:220–252, 1977.

[22] R. Peyret and T. D. Taylor. *Computational methods for fluid flow.* Springer series in computational physics. Springer-Verlag, New York, Heidelberg, Berlin, 1985.

[23] A. Prosperetti. Motion of two superimposed viscous fluids. *Physics of Fluids*, 24:1217–1223, 1981.

[24] E. G. Pucket, A. S. Almgren, J. B. Bell, D. L. Marcus, and W. J. Rider. A High-Order Projection Method for Tracking Fluid Interfaces in Variable Density Incompressible Flows. *Journal of Computational Physics*, 130:269–282, 1997.

[25] W. R. Rider, D. B. Kothe, S. J. Mosso, J. H. Cerutti, and J. I. Hochstein. Accurate Solution Algorithms for Incompressible Multiphase Flows. *Proceedings of the 33rd AIAA Aerospace Science Meeting and Exhibit*, AIAA-95-0699, Reno, NV, Jan. 1995.

[26] G. Ryskin and L. G. Leal. Numerical Solution of Free-Boundary problems in Fluid Mechanics, Part 2. Buoyancy-Driven Motion of a Gas Bubble Through a Quiescent Liquid. *Journal of Fluid Mechanics*, 148:19–35, 1984.

[27] Popinet S. and Zaleski S. A front-tracking algorithm for accurate representation of surface tension. *International Journal for Numerical Methods in Fluids*, 30(6):775–793, 1999.

[28] R. Scardovelli and S. Zaleski. Direct Numerical Simulation of Free-Surface and Interfacial Flow. *Annu. Rev. Fluid Mech.*, 31:567–603, 1999.

[29] T. Schneider. Zur Flammenverfolgung in schwachkompressiblen reaktiven Strömungen. *Dissertation RWTH Aachen*, submitted.

[30] T. Schneider, N. Botta, K. J. Geratz, and R. Klein. Extension of finite volume compressible flow solvers to multi-dimensional, variable density zero Mach number flows. *Journal of Computational Physics*, 155:248–286, 1999.

[31] T. Schneider and R. Klein. Overcoming mass losses in Level-Set-based interface tracking schemes. *Second International Symposium on Finite Volumes for Complex Applications – Problems and Perspectives*, July 19-22, 1999, Berlin, Germany.

[32] V. Smiljanovski, V. Moser, and R. Klein. A capturing-tracking hybrid scheme for deflagration discontinuities. *Combustion Theory and Modelling*, 2(1):1997, 1997.

[33] M. Sussman, A. S. Almgren, J. B. Bell, P. Colella, L. H. Howell, and M. L. Welcome. An adaptive level set approach for incompressible two-phase flow. *Journal of Computational Physics*, 148:81–124, 1999.

[34] M. Sussman and E. Fatemi. An efficient, interface preserving level set re-distancing algorithm and its application to interfacial incompressible fluid flow. *SIAM Journal of Scientific Computing*, 20(4):1165–1191, 1999.

[35] M. Sussman, E. Fatemi, P. Smereka, and S. Osher. An Improved Level Set Method for Incompressible Two-Phase Flows. *Computers & Fluids*, 27:663–680, 1998.

[36] M. Sussman, Smereka P., and Osher S. A level set approach for computing solutions of incompressible two-phase flow. *Journal of Computational Physics*, 114:146–159, 1994.

[37] P. Terhoeven. *Ein numerisches Verfahren zur Berechnung von Flammenfronten bei kleiner Mach-Zahl.* Dissertation, RWTHAachen, 1998.

[38] G. Tryggvason, B. Bunner, O. Ebrat, and W. Tauber. Computations of Multiphase Flows by a Finite Difference/Front Tracking Method. I. Multi-Fluid Flows. 29th computational fluid dynamics lecture series, Von Karman Institute for Fluid Dynamics, 1998-03.

[39] S. O. Unverdi and G. Tryggvason. A Front Tracking Method for Viscous, Incompressible Multi-Fluid Flow. *Journal of Computational Physics*, 100:25–37, 199.